

See discussions, stats, and author profiles for this publication at: <https://www.researchgate.net/publication/236198357>

# Enhanced Hematite Water Electrolysis Using a 3D Antimony-Doped Tin Oxide Electrode

ARTICLE in ACS NANO · APRIL 2013

Impact Factor: 12.88 · DOI: 10.1021/nn400744d · Source: PubMed

CITATIONS

18

READS

65

8 AUTHORS, INCLUDING:



Navid Soheilnia

University of Toronto

40 PUBLICATIONS 594 CITATIONS

SEE PROFILE



Paul O'Brien

University of Toronto

31 PUBLICATIONS 390 CITATIONS

SEE PROFILE



Michael G Helander

University of Toronto

104 PUBLICATIONS 2,221 CITATIONS

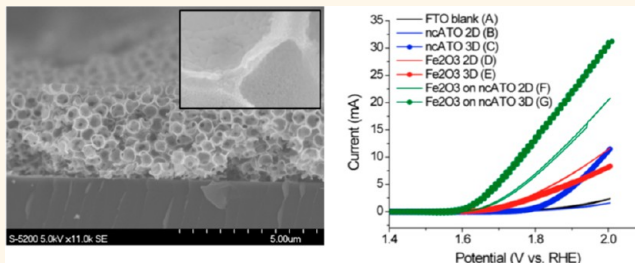
SEE PROFILE

# Enhanced Hematite Water Electrolysis Using a 3D Antimony-Doped Tin Oxide Electrode

Jonathon Moir, Navid Soheilnia, Paul O'Brien, Abdinoor Jelle, Claudia M. Grozea, Daniel Faulkner, Michael G. Helander, and Geoffrey A. Ozin\*

Materials Chemistry and Nanochemistry Research Group, Centre for Inorganic and Polymeric Materials, Department of Chemistry, University of Toronto, 80 St. George Street, Toronto, Ontario M5S 3H6, Canada

**ABSTRACT** We present herein an example of nanocrystalline antimony-doped tin oxide (nc-ATO) disordered macroporous “inverse opal” 3D electrodes as efficient charge-collecting support structures for the electrolysis of water using a hematite surface catalyst. The 3D macroporous structures were created *via* templating of polystyrene spheres, followed by infiltration of the desired precursor solution and annealing at high temperature. Using cyclic voltammetry and electrochemical impedance spectroscopy, it was determined that the use of this 3D transparent conducting oxide with a hematite surface catalyst allowed for a 7-fold increase in active surface area for water splitting with respect to its 2D planar counterpart. This ratio of surface areas was evaluated based on the presence of oxidized trap states on the hematite surface, as determined from the equivalent circuit analysis of the Nyquist plots. Furthermore, the presence of nc-ATO 2D and 3D “underlayer” structures with hematite deposited on top resulted in decreased charge transfer resistances and an increase in the number of available active surface sites at the semiconductor–liquid junction when compared to hematite films lacking any nc-ATO substructures. Finally, absorption, transmission, and reflectance spectra of all of the tested films were measured, suggesting the feasibility of using 3D disordered structures in photoelectrochemical reactions, due to the high absorption of photons by the surface catalyst material and trapping of light within the structure.



**KEYWORDS:** water splitting · hematite · macroporous electrode · inverse opal · transparent conducting oxide · impedance spectroscopy · cyclic voltammetry

Nanomaterials are synonymous with high surface area, a characteristic that is of paramount importance in the areas of catalysis, photocatalysis, and electrochemistry.<sup>1–4</sup> One of the most sought-after reactions that benefits from these large surface area nanomaterial catalysts is the splitting of water into oxygen and hydrogen gases, which can be achieved through the use of either electrical energy, light energy, or a combination of the two.<sup>5–8</sup> In the water-splitting system, the oxygen-evolving reaction is the most studied of the two half reactions (the other being the hydrogen-evolving reaction), due to the complex kinetics and high overpotentials required to initiate it.<sup>6</sup> Water electrolysis can be performed quite simply using metal alloy electrodes in alkaline solutions; however, a large electrical energy input is required to initiate and maintain the reaction.<sup>5</sup>

By subsidizing the electrical energy input using an alternative form of energy, such as light, the applied potential required to maintain the reaction can be minimized (photoelectrochemical water splitting) or even eliminated completely (photocatalytic water splitting).<sup>7,8</sup> Since the first report of photoelectrochemical water splitting by Honda and Fujishima in 1972,<sup>9</sup> innumerable materials (both nano and bulk) have been tested to this end, with the aim of being able to produce hydrogen gas as an alternative fuel source using cheap and abundant catalyst materials. Researchers have attempted to improve the efficiency of various semiconductor photoactive materials *via* nanostructuring, doping, heterojunctions, and surface modifications, among others.<sup>1,10–14</sup> However, water splitting remains a difficult and energy-intensive process.

\* Address correspondence to gozin@chem.utoronto.ca.

Received for review February 13, 2013 and accepted April 12, 2013.

Published online April 12, 2013  
10.1021/nn400744d

© 2013 American Chemical Society

As such, high surface area materials are of the utmost importance in water-splitting applications. Many examples of high surface area materials have been reported in the literature for water electrolysis, specifically a number of 3D "inverse opal" structures.<sup>1,12,14–17</sup> These structures are created using either polystyrene or silica opal templates which are then infiltrated with the desired precursor before being removed *via* etching or annealing processes, leaving the infiltrated skeleton structure or inverse opal structure. Not only do these structures have extremely high surface areas, but they are also privy to photonic crystal effects, which have been shown to enhance the photoactivity of a given material for water oxidation by decreasing the group velocity of light within the photonic structure.<sup>16–18</sup>

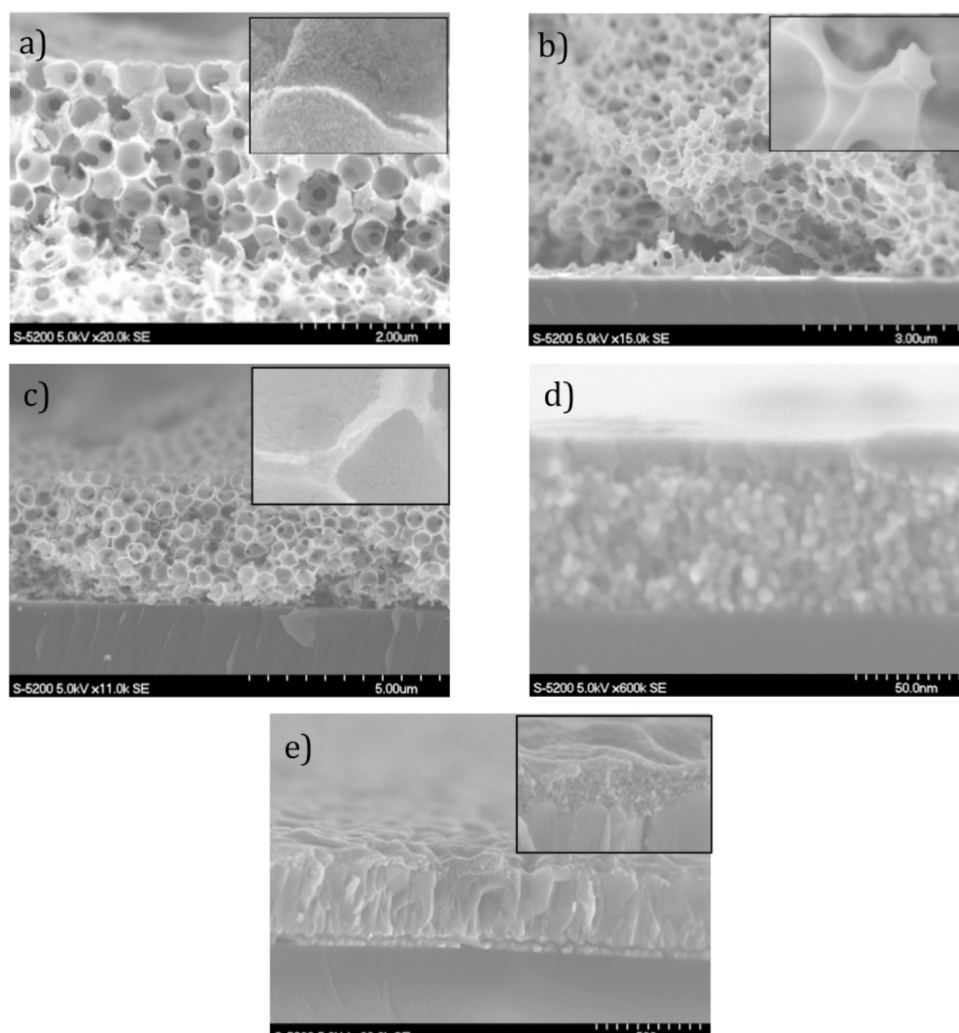
In this report, we explore the use of hematite ( $\alpha\text{-Fe}_2\text{O}_3$ ) as a water oxidation catalyst in 2D planar and 3D disordered macroporous (inverse opal) structured morphologies, created using polystyrene opals as a template. Although hematite is a well-documented catalyst for water oxidation, specifically as a photoactive semiconductor material for photoelectrochemical water splitting,<sup>1,19–23</sup> it is plagued by a short charge diffusion length, resulting in poor charge transport through the material. As a result, the total current outputs for the 2D planar and 3D macroporous  $\alpha\text{-Fe}_2\text{O}_3$  films tested in this study were found to be almost identical, with the 3D structure actually showing a *lower* current output at higher potentials due to a lower active surface area and potentially deleterious mass transport effects. Therefore, in order to increase the surface area (and hence output current) of  $\alpha\text{-Fe}_2\text{O}_3$  films under (photo)anodic conditions, nanocrystalline antimony-doped tin oxide (nc-ATO) macroporous structures were constructed in order to enhance charge collection in 3D morphologies. Not only is nc-ATO highly conductive but it is also transparent to visible light, making it a desirable material for expanding electrodes into three dimensions without sacrificing light absorption in photoelectrochemical applications.<sup>24,25</sup> To this end, macroporous (inverse opal) structures of nc-ATO were prepared using polystyrene opals as a template and subsequently coated with hematite. The nc-ATO by itself is a poor water oxidation catalyst, as demonstrated herein by its low activity and high overpotentials. However, when 3D macroporous structures of nc-ATO were coated with  $\alpha\text{-Fe}_2\text{O}_3$ , the output current increased dramatically, owing to the enhancement in charge collection by the nc-ATO 3D structure and the higher kinetic activity of the hematite material.

All of these activity and surface area enhancements were evaluated using cyclic voltammetry (CV) and electrochemical impedance spectroscopy (EIS). The voltammograms were evaluated based on a macroscopic theory of electrode kinetics, in both the

non-Faradaic and Faradaic potential regions. These results were compared to EIS measurements at applied potentials of approximately 1.00 and 1.65 V vs RHE. The data were fit to a Randles' equivalent circuit, and the capacitances and charge transfer resistances were evaluated for all of the tested films. Results suggest that the hematite supported by the 3D nc-ATO macroporous structure showed a 7-fold increase in active surface area with respect to its planar 2D counterpart, owing to an increase in available active surface sites on the hematite catalyst. The benefit of a bilayer configuration of the semiconductors is also addressed with respect to increased activity and decreased overpotential, which relates to the CV and EIS measurements. In addition, absorption, transmission, and reflectance measurements were performed on the films using an integrating sphere to determine the suitability of the disordered macroporous inverse opal structures for photoelectrochemical water-splitting applications.

## RESULTS AND DISCUSSION

**Construction of Planar (2D) and Macroporous (3D) Films.** The macroporous structures were constructed as described in the Methods section. X-ray diffraction (XRD) measurements are available in the Supporting Information and confirm hematite (corundum) and cassiterite crystallographic phases for  $\alpha\text{-Fe}_2\text{O}_3$  and nc-ATO, respectively. For the nc-ATO 2D and 3D films, a nanocrystalline form of the transparent conducting oxide was chosen due to its higher porosity and lower charge transport resistance than a similar ATO structure derived from a sol–gel precursor.<sup>24</sup> Figure 1 displays SEM cross-sectional images of the disordered inverse opal structures. The effect of the necking is clearly evident from the tunnels and holes in the structure, allowing for extremely high porosity and infiltration of electrolyte. The insets in all of the images show close-ups of the materials. Figure 1a displays the well-maintained nanocrystallinity of the ATO 3D structure, whereas the hematite 3D structure in Figure 1b is dense and uniform (also evidenced by the sharp peaks in the XRD patterns; see Supporting Information). Upon deposition of  $\alpha\text{-Fe}_2\text{O}_3$  onto the walls of the 3D nc-ATO inverse opals, the structure and porosity are maintained at the micro- and macroscale (see Figure 1c). Close examination of the inset in Figure 1c shows that the two materials are clearly distinguishable at the nanoscale. Because the hematite was wet impregnated onto the walls of the nc-ATO macroporous structure, it forms a much denser film (about 15–20 nm in thickness) with small undulations in the surface, as shown in the inset of Figure 1c (a similar result is shown for the spin-coated hematite film in Figure 1e). The high degree of disorder evident in all of the macroporous samples can likely be attributed to a combination of factors, including the method of deposition (doctor-blading) and the polydispersity of the opals (see Supporting Information



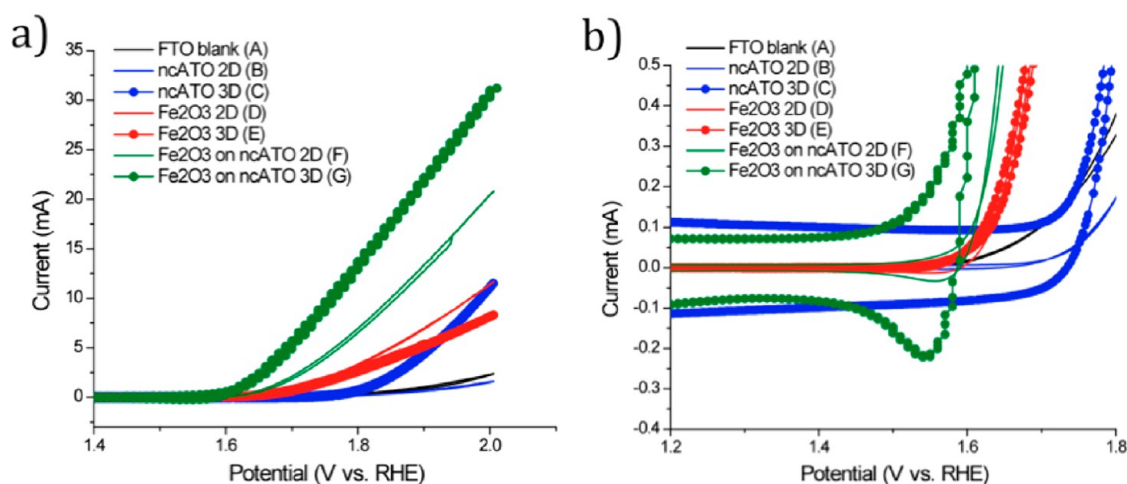
**Figure 1.** SEM cross-sectional images of planar and inverse opal structures: (a) nc-ATO inverse opals only (nc-ATO 3D); (b)  $\alpha$ -Fe<sub>2</sub>O<sub>3</sub> inverse opals only (Fe<sub>2</sub>O<sub>3</sub> 3D); (c)  $\alpha$ -Fe<sub>2</sub>O<sub>3</sub> deposited on the walls of the nc-ATO inverse opals (Fe<sub>2</sub>O<sub>3</sub> on nc-ATO 3D). Note that these first three samples are deposited on silicon wafers. The insets show the materials at a closer range, demonstrating the nanocrystalline nature of the ATO and the dense nature of the  $\alpha$ -Fe<sub>2</sub>O<sub>3</sub>. The inset in (c) clearly shows the contrast between the two materials when one is deposited on the other. (d) Planar sample of  $\sim$ 20 nm of  $\alpha$ -Fe<sub>2</sub>O<sub>3</sub> spin-coated onto a  $\sim$ 80 nm layer of nc-ATO (Fe<sub>2</sub>O<sub>3</sub> on nc-ATO 2D), deposited on a silicon wafer. (e) Same sample as (d) but prepared on an FTO substrate. Note the undulating surface morphology that gives rise to an inherent surface roughness in the case of the FTO substrate.

Figure S5). Doctor-blading was chosen as the method of deposition due to its speed and efficiency, yet the resulting disorder may, in fact, be advantageous for enhanced light absorption due to multiple light scattering within the structure (see Figure 6), a necessary requirement in photoelectrochemical applications.<sup>26</sup> Figure 1d,e shows the deposition of a 2D planar film of  $\alpha$ -Fe<sub>2</sub>O<sub>3</sub> ( $\sim$ 20 nm) onto a 2D planar film of nc-ATO ( $\sim$ 80 nm) on both silicon and FTO substrates, respectively. Note that the high surface roughness of the FTO substrate results in an undulating surface morphology *versus* the smooth, flat surface provided by the silicon wafer.

**Cyclic Voltammetry.** In order to evaluate the activity of the semiconductor films for water oxidation, cyclic voltammetry was employed using a three-electrode setup, as described in the Methods section. Figure 2

displays the cyclic voltammograms recorded for the 2D planar and 3D macroporous films. From these plots, a number of interesting observations can be made. First, it is clear in Figure 2a that the FTO and nc-ATO planar films are poor water oxidation catalysts (curves A and B, respectively), as demonstrated by their low current densities and high overpotentials. However, upon expansion of the nc-ATO 2D planar film into three dimensions (the nc-ATO 3D macroporous film, curve C), a substantial increase in current is observed, a result of the tremendous increase in surface area available for water oxidation over the same geometric (apparent) surface area. However, despite this increase, the high overpotential inherent to the material remains the same.

Deposition of the planar hematite ( $\alpha$ -Fe<sub>2</sub>O<sub>3</sub>) film (curve D) onto FTO, on the other hand, not only results in a substantial shift in the overpotential to less positive



**Figure 2.** (a) Cyclic voltammograms of various films of FTO,  $\alpha$ - $\text{Fe}_2\text{O}_3$ , nc-ATO, and  $\alpha$ - $\text{Fe}_2\text{O}_3$  on nc-ATO. All of the  $\alpha$ - $\text{Fe}_2\text{O}_3$  and nc-ATO films and all of the composite films were deposited on FTO. Films were measured in 1.0 M NaOH in the dark vs Hg/HgO and adjusted to the reversible hydrogen electrode (RHE). (b) Zoom-in of panel a, close to the level of zero current. Non-Faradaic currents are clearly evident for films containing nc-ATO inverse opals, due to the increased surface area and capacitance of the films. Reduction peaks are evident only for films containing  $\alpha$ - $\text{Fe}_2\text{O}_3$ , suggested to be the result of the reduction of oxidized surface species.

potentials but also results in a significant increase in the current density for the same geometric surface area as the FTO and nc-ATO 2D planar films. The increase in both cases is a result of the inherently higher activity of the  $\alpha$ - $\text{Fe}_2\text{O}_3$  toward water oxidation (see the description below regarding the Tafel plot in Figure 4, the Tafel slopes displayed in Table 2, and the section entitled Electrochemical Impedance Spectroscopy for more details).

Expansion of the hematite film into three dimensions would be highly desirable, not only to increase the ratio of real surface area to geometric surface area but also to increase the absorption of light by the semiconductor for photoelectrochemical applications. However, it is expected that the resulting enhancement in current output for a 3D structure of pure  $\alpha$ - $\text{Fe}_2\text{O}_3$  would be minimal, due to the inherently poor charge transport abilities of the material. This is clearly the case for the 3D macroporous hematite film represented by curve E in Figure 2a. Not only does the 3D  $\alpha$ - $\text{Fe}_2\text{O}_3$  film show similar activity to the planar 2D hematite film, but in fact, its current output is actually *lower* than its planar counterpart at higher potentials. This is likely due to both lower active surface area and mass transport effects within the macroporous film at higher applied potentials. In the former case, areas of disconnect between the hematite structure and the FTO substrate (see Figure 1b) would result in lower surface coverage of the electrode, yielding lower output currents. This could be compounded by areas of the structure (*i.e.*, the walls) wherein a greater amount of material is deposited in the direction perpendicular to the substrate surface. In the latter case, mass transport limitations of the reactants and products through the tortuous 3D structure could also slow the oxidation of water at higher applied potentials (where electron transfer is no longer rate-limiting) and similarly impede

the reaction (this is also confirmed in the Tafel analysis shown in Figure S8). It is obvious then that the remainder of the 3D structure is useless toward water oxidation, and only the part of the hematite structure closest to the FTO substrate will be electrochemically active.

Therefore, in order to increase the real surface area for hematite over a given geometric surface area,  $\alpha$ - $\text{Fe}_2\text{O}_3$  was deposited onto the walls of a 3D nc-ATO macroporous inverse opal structure (Figure 1c), and the results of electrolysis are given by curve G in Figure 2a. This structure shows a substantial increase in activity compared to all of the other films. This increase is associated with the enhanced surface area provided by the nc-ATO 3D macroporous support structure and the ability to make use of all of the deposited hematite (photo)catalyst. Additionally, unlike in the case of the 3D macroporous pure hematite structure (curve E), mass transport is less of an issue due to the strong electronic communication throughout the structure provided by the nc-ATO inverse opal support.

When considering Figure 2a, it is interesting to note that the hematite film deposited onto the 2D planar film of nc-ATO has a slightly higher activity than the hematite film deposited directly onto the FTO glass electrode, despite the fact that their geometric surface areas are the same. An initial assumption would be that the roughness of the planar nc-ATO film could be slightly greater than the roughness of the FTO glass electrode by itself (since they are not, strictly speaking, “flat”). However, AFM measurements (see Figures S6 and S7) show that the opposite situation has arisen, wherein the surface roughness of the hematite film on its own is actually *greater* than the surface roughness of the bilayer film, suggesting the possibility that an alternative effect is responsible for the enhanced activity (see the Electronic Effects on Film Activity section below).



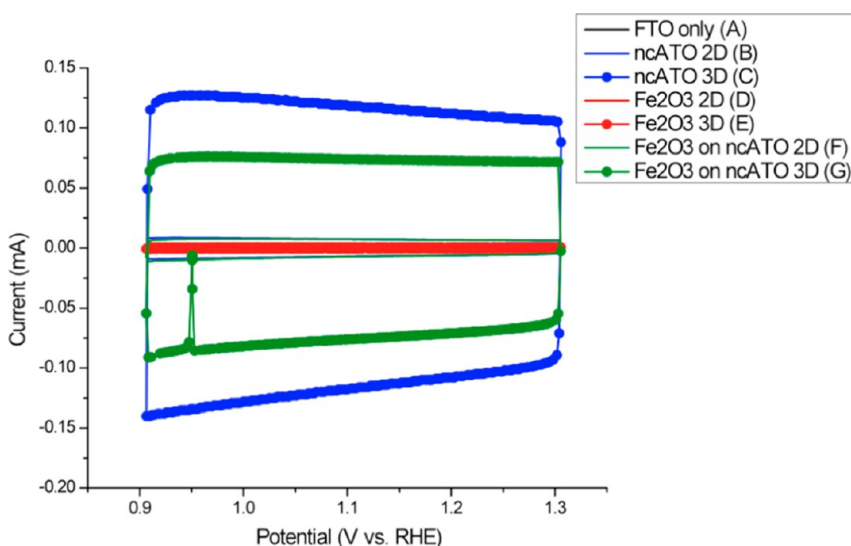


**Figure 3.** Cyclic voltammograms of all films, scanned through the non-Faradaic potential region. A total of three scans were performed for each film, with the final scan plotted in the figure. The small peak in curve G is a result of the instrument and not of the film.

Other aspects of Figure 2a reveal important clues as to the surface area enhancements for the various films. Upon closer examination of the voltammograms, reduction peaks are evident near the level of zero current for films containing  $\alpha$ - $\text{Fe}_2\text{O}_3$ , as shown in Figure 2b. These quasi-reversible peaks have recently been suggested to be the result of higher valence iron surface sites (most likely Fe(IV)) that are active in the oxidation of water and glucose at the hematite surface.<sup>27,28</sup> The reduction peak in Figure 2b for the film of  $\alpha$ - $\text{Fe}_2\text{O}_3$  deposited onto the walls of the 3D macroporous nc-ATO structure is substantially larger than any of the other films containing iron oxide and is strong evidence for the high number of active surface states accessible when using a 3D electrode even when accounting for the non-Faradaic contribution to the current.

Evaluation of the non-Faradaic part of Figure 2a, from 0.9 to 1.3 V, also reveals important properties of these semiconductor films.<sup>29</sup> To that end, a second set of cyclic voltammograms was recorded from 0.9 to 1.3 V vs RHE, at the same scan rate, in order to evaluate the capacitive nature of the films. The resulting spectra are shown in Figure 3 (the small peak at 0.95 V is a result of the instrument and not of the films themselves). Modeling of these current profiles as a function of potential over a region of non-Faradaic activity can be done using a simple RC circuit (see Supporting Information for full description).<sup>30</sup> Although this model applies primarily to ideal polarized electrodes coupled with ideal reversible electrodes, the method is instructive and the results closely match the capacitance values measured using EIS in the same potential region. Within the plateau region of the voltammograms, the exponential decay function (eq S1) simplifies to the product of the scan rate ( $\nu$ , in V/s) and the

**TABLE 1.** Overall Relative Capacitance Measurements for All of the Tested Films As Derived from the Exponential Decay Modeling of the Curves in Figure 3, Normalized to the Measured Capacitance of the Blank FTO Electrode<sup>a</sup>

film	$C_N$ (rel)
FTO only (A)	$1.0 \pm 0.5$
nc-ATO 2D (B)	$14 \pm 5$
nc-ATO 3D (C)	$210 \pm 70$
$\text{Fe}_2\text{O}_3$ 2D (D)	$1.0 \pm 0.5$
$\text{Fe}_2\text{O}_3$ 3D (E)	$1.0 \pm 0.5$
$\text{Fe}_2\text{O}_3$ on nc-ATO 2D (F)	$12 \pm 4$
$\text{Fe}_2\text{O}_3$ on nc-ATO 3D (G)	$130 \pm 40$

<sup>a</sup> The large errors associated with these measurements are a result of the difficulty in modeling the films with low non-Faradaic output currents.

capacitance ( $C_N$ , in F), as follows:

$$I \approx \nu C_N \quad (1)$$

From this relationship, a ratio of the currents within this plateau region will yield a ratio of the capacitances of the various films and hence a ratio of the surface area resulting from non-Faradaic processes only. Table 1 shows the relative capacitances of all of the films calculated by modeling the curves in Figure 3 using the exponential decay relation (equation S1), which yields eq 1 over long time periods. From these results, it is clear again that the films containing nc-ATO (in either a 2D or 3D form) have a higher surface area (capacitance) compared to the bare FTO glass electrode, and that the 3D nc-ATO film has about 15 times the charge density of its 2D nc-ATO counterpart. Even upon deposition of hematite onto the nc-ATO films (2D or 3D), the capacitance of the 3D film remains quite high ( $\sim 10$  times higher) compared to the 2D version. However, there is a high error associated with this method, which is a result of the difficulty of

modeling the FTO glass electrode (curve A in Figure 3, essentially overlaid with the potential axis) using this exponential decay function, to which all of the other films are compared. Other films that had non-Faradaic current densities close to zero were similarly difficult to model (curves D and E in Figure 3) and resulted in high errors, as well.

It is important to note that the use of a simple RC circuit in modeling a complex film, especially a nanocrystalline semiconductor 3D macroporous structure, is a highly simplified approximation to the real system.<sup>31</sup> The capacitance considered in this case is a total capacitance, with contributions from the semiconductor space-charge region and the Helmholtz double layer,<sup>30–33</sup> although generally the contribution of the latter can be ignored due to the short distances over which the electrical double layer exists (we assume this even in the case of the highly doped nc-ATO and FTO transparent conductive oxide semiconductors).<sup>31,34</sup> From this simplification, it can therefore be assumed that the capacitance values in Table 1 are primarily the result of charge buildup in the space-charge regions of the semiconductor materials. However, a comparison of the measured capacitances of different semiconductors (nc-ATO and  $\alpha$ -Fe<sub>2</sub>O<sub>3</sub>) is difficult to do, given that the width of the space charge region within each material will be a function of the doping level in the semiconductors and of the mismatch between the Fermi levels of the materials and the electrolyte.<sup>35</sup> These conditions will be different in the case of nc-ATO and  $\alpha$ -Fe<sub>2</sub>O<sub>3</sub>, and so a ratio of capacitances is not necessarily representative of a surface area enhancement. As such, a better comparison is made by taking the ratio of capacitances in Table 1 between the 2D and 3D films of the same semiconductor material(s) (comparing 2D nc-ATO with 3D nc-ATO (curves B and C in Figure 3), 2D  $\alpha$ -Fe<sub>2</sub>O<sub>3</sub> with 3D  $\alpha$ -Fe<sub>2</sub>O<sub>3</sub> (curves D and E in Figure 3), and the 2D composite film with the 3D composite film (curves F and G in Figure 3)). Again, the 3D structures containing the conductive nc-ATO supports show far greater capacitances than their 2D counterparts, up to 10–15 times the charge storage density of their planar versions. In the case of the 2D and 3D films containing only hematite, the capacitance values are essentially identical, which is consistent with the results of the CV measurements in Figure 2a described above.

As an aside, the total capacitance at the working electrode (the electrical double layer and the space charge region in the semiconductor) generally changes as a function of applied potential, and so the capacitance values measured using the above model are averaged over the range of potentials shown in Figure 3.<sup>30,34</sup> This is the point at which electrochemical impedance spectroscopy becomes an important tool in capacitance and resistance determination in thin films, as the sinusoidal perturbation of a DC potential

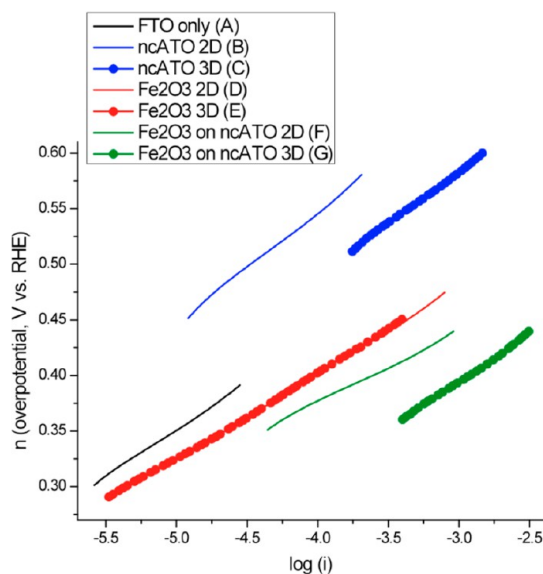


**Figure 4.** Linear Tafel plots of all films tested. Note that curves D and E overlap almost identically.

over a small range allows for a more accurate determination of these semiconductor properties. Nevertheless, the simple RC circuit model described above yields an approximate comparison between the capacitances of the 2D and 3D films and, encouragingly, closely matches the results of the impedance measurements determined at an applied potential of 1.00 V vs RHE and displayed in Table 3. Additionally, due to the presence of only one semicircle in the Nyquist plots at low frequencies the impedance measurements could only be modeled using a simple Randles' equivalent circuit (shown in Figure 5).<sup>27,32,36</sup> The advantage here, however, is that a simple correlation can be made between the RC series circuit described above and the Randles' equivalent circuit displayed in Figure 5a, which differs only by the presence of a charge transfer process. The above model is therefore beneficial to our discussion, and further analysis is given in the section entitled Electrochemical Impedance Spectroscopy.

**Tafel Plots.** To further evaluate surface area enhancements from the 3D conductive nc-ATO support structures, the Faradaic region of the voltammograms in Figure 2a was also evaluated (from 1.5 to 2.0 V applied potential), resulting in Tafel relationships for all of the films, plotted in Figure 4. The Tafel equation (equation S5; see Supporting Information for full description) describes the relationship between the overpotential  $\eta$  and the logarithm of the current  $i$ .<sup>37</sup> Tafel plots (plots of  $\eta$  vs  $\log(i)$ ), shown in Figure 4, are important metrics for water oxidation catalysts and can yield important information about electronic and geometric enhancements in activity for a given set of electrodes/catalysts, even if only on a semiquantitative basis.<sup>38</sup> In general, a decrease in the slope of the curve is representative of a beneficial electronic effect. Similarly, an increase in the exchange current (or the

**TABLE 2. Tafel Slopes and Exchange Current Densities, Determined from Linear Extrapolations of the  $\eta$  vs  $\log(I)$  Data, Shown in Figure 3,<sup>a</sup>**

film	slope (mV/decade)	Exchange Current, relative exchange $i_0$ (A)	current	$R^2$
FTO only (A)	84.2	$6.71 \times 10^{-10}$	1.00	0.999
nc-ATO 2D (B)	104	$5.45 \times 10^{-10}$	0.812	0.996
nc-ATO 3D (C)	92.5	$4.99 \times 10^{-10}$	0.744	0.999
Fe <sub>2</sub> O <sub>3</sub> 2D (D)	74.9	$4.08 \times 10^{-10}$	0.607	0.999
Fe <sub>2</sub> O <sub>3</sub> 3D (E)	76.8	$5.81 \times 10^{-10}$	0.866	0.998
Fe <sub>2</sub> O <sub>3</sub> on nc-ATO 2D (F)	63.7	$1.25 \times 10^{-10}$	0.186	0.998
Fe <sub>2</sub> O <sub>3</sub> on nc-ATO 3D (G)	85.8	$2.52 \times 10^{-8}$	37.5	0.998

<sup>a</sup> Slopes and exchange currents were taken from the first (or middle) linear portion of each data set in order to do a proper comparison. The accuracy of each fitting ( $R^2$ ) is given in the last column and was extremely good for all films tested.

intercept of the line with the potential axis) is the result of a beneficial geometric effect or an enhanced surface area. Furthermore, mechanistic information can often be deduced from Tafel slopes, depending on the reaction and the shape of the Tafel plots.<sup>39–42</sup>

On the basis of the definition of exchange current (eq S6), it can be reasoned that a surface area ratio (or the surface area enhancement) between two electrodes can be made by comparing the exchange currents of the films, but only under the condition that their rate constants and reduced surface species concentrations ( $k_{\text{rds}}^0$  and  $C_{\text{R}}(0,t)$ , respectively) are the same. Table 2 shows the relative exchange currents with respect to the bare FTO electrode, which assumes that these constants are the same for all of the electrodes, therefore giving a relative evaluation of the surface areas of all seven films. Again, this assumption may be limited, given that surface species concentrations and rate constants may be different from one material to the next, a similar phenomenon to that described above pertaining to the capacitance of different semiconductor materials. A better evaluation is again the comparison between the same materials in 2D and 3D configurations, for which it is safer to assume that the rate constants and  $C_{\text{R}}(0,t)$  values will be the same. Hence, the ratio of exchange currents between curves B and C, D and E, and F and G (shown in Figure 4) should yield a more accurate comparison of the activity enhancement due to increased surface area.

To this end, Table 2 displays the exchange currents and relative exchange currents for all of the films tested in this study. When comparing only the curves that represent the same material in 2D and 3D morphologies, the relations are sound in two of the three cases. For 2D and 3D films of hematite (curves D and E), exchange currents (and Tafel slopes) are nearly identical, as expected for a material with poor charge transport capabilities, and again consistent with all of the other electrochemical measurements. In the case of the 2D and 3D composite (“bilayer”) structures that

contain both nc-ATO and hematite, the surface area increases by nearly 2 orders of magnitude for the 3D structure (curve G) when compared to the 2D planar bilayer film (curve F), as expected. However, when comparing the 2D and 3D nc-ATO films (curves B and C), there is a negligible surface area enhancement observed. This is not expected, given the capacitance measurements from the cyclic voltammograms and the EIS measurements. The most likely reason for this anomaly is the fact that the Tafel slopes derived for these two films are slightly different, allowing the plots to converge to the same exchange current at an overpotential of zero.

When considering Tafel slopes, although measurements can vary broadly, they can generally yield important information regarding beneficial electronic properties as well as mechanistic insight into electron transfer processes at the catalyst surface. A Tafel slope of about 40 mV/decade is expected for a rate-determining step involving the oxidation of an OH surface species and is generally observed in the lower overpotential region of a water oxidation Tafel plot.<sup>40–42</sup> Conversely, a Tafel slope of ~120 mV/decade is expected for a rate-determining step involving the initial oxidation of an OH<sup>−</sup> anion at the surface of the electrode/catalyst and is generally observed at higher overpotentials. However, in the present case, the measured Tafel slopes vary between 60 and 105 mV/decade. This discrepancy could be the result of a number of contributing factors. For one, the theoretical values listed above (40 and 120 mV/dec) assume a transfer/symmetry coefficient of 0.5.<sup>42–44</sup> Deviations from this expected value, such as with higher Tafel slopes, could result in higher transfer coefficients and a shift in the reaction coordinate.<sup>37,45</sup> Tafel slopes have been shown to deviate widely depending on the preparation of the catalyst, the exposed surface, the crystallinity, and the electrolysis conditions.<sup>40,46–48</sup>

It is also possible that the Tafel slopes presented herein are the result of a different mechanism, such as a classical two-electron process<sup>39,43</sup> or a mechanism requiring a chemical rearrangement step,<sup>42</sup> both of which would result in a theoretical slope of 60 mV/decade, which closely matches many of the slopes displayed in Table 2. However, further mechanistic studies would be required to validate this assumption. In general, it is clear that a trend moving from curves A through G shows a decrease in the Tafel slope, meaning that the deposition of hematite onto the transparent conducting oxide surfaces results in enhanced activity toward water oxidation. Additionally, it is important to note that curves B and C exhibit linear Tafel relations at much higher overpotentials than the other five films, suggesting a closer relationship to the one-electron oxidation of a surface hydroxyl anion with a theoretical slope of 120 mV/decade, as stated above. Not only that, but this could also imply a change in the



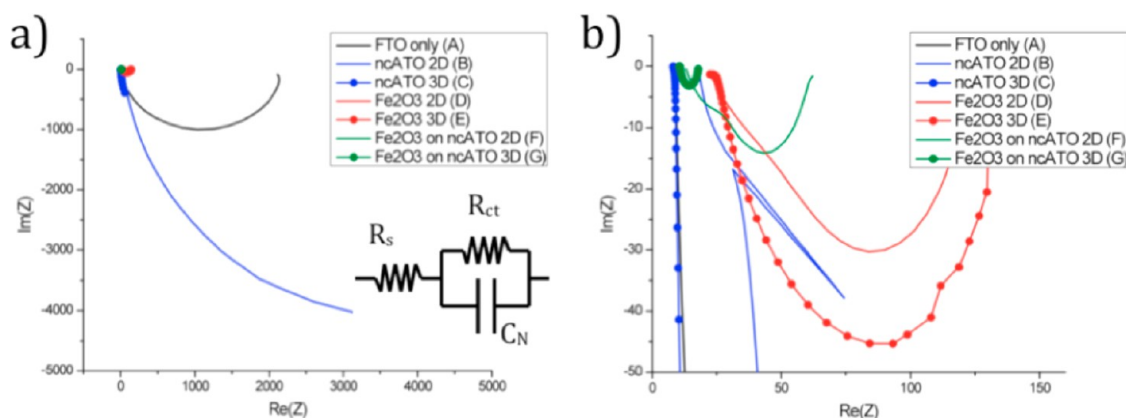


**Figure 5.** (a) Nyquist plot of all films tested at 1.65 V vs RHE. The Randles' equivalent circuit used to model the data is displayed in the inset. (b) Zoom-in close to the  $\text{Re}(Z)$  axis, showing the semicircles associated with the films containing hematite.

free energy of binding of intermediates at the surface of the nc-ATO when compared to the hematite and FTO surfaces, which would affect not only the thermodynamic overpotential but inevitably the kinetic barriers as well.<sup>49</sup> Nonetheless, the Tafel slopes shown in Table 2 closely match reported values for both hematite<sup>27</sup> and other (mixed) metal oxide catalysts<sup>40,41,50</sup> and are useful for comparing water oxidation catalysts over large ranges of current and under similar electrolysis conditions.

**Electrochemical Impedance Spectroscopy (EIS).** In order to more accurately evaluate geometric and electronic enhancements between all of the films tested in this study, electrochemical impedance spectroscopy (EIS) was used to determine the capacitances and resistances within the water-splitting cells.<sup>27,32</sup> This not only helped in determining the relative surface area enhancements but also has given insight into the reason for the enhanced activity and decreased overpotential displayed by the films of  $\alpha\text{-Fe}_2\text{O}_3$  deposited onto 2D and 3D structures of nc-ATO. The films were tested at two different potentials (1.00 and 1.65 V vs RHE), with the Nyquist plots acquired at 1.65 V displayed in Figure 5 (see Supporting Information for Nyquist plots for the lower applied potential). The Nyquist plots were modeled using a Randles' equivalent circuit (shown in Figure 5), which is traditionally used for semiconductor samples tested in the dark and for which only one semicircle is present.<sup>27,32</sup> The potential values were selected based on the activity of the films at the potential in question: one measurement (1.00 V) in the non-Faradaic region, and one measurement (1.65 V) in the Faradaic region, in order to discern any surface area and charge transfer effects that could be accounting for the increased activity in the films. It should be noted that, although a capacitor is displayed in the equivalent circuit in Figure 5a, a constant phase element (CPE) was used in the fitting, in order to account for inhomogeneities at the surfaces of the films. However, the exponential parameters fitted using the computer software and displayed in Table S1 in the Supporting Information were generally found to

be close to unity, confirming the validity of the capacitor element in the circuit.<sup>51</sup>

For the capacitance values measured at 1.00 V vs RHE (shown in Table 3), the relative capacitances are almost identically matched to those determined in Table 1 using the exponential decay model, a testament to the consistency of the films and the model. In this case, at a potential where non-Faradaic currents are dominant, the Randles' equivalent circuit breaks down into a simple series RC circuit, as discussed above, such that the charge transfer resistance ( $R_{ct}$ ) is too high for any appreciable current to pass through the semiconductor–liquid junction (SCLJ). In this case, the Nyquist plots result in straight lines (see Figures S9 and S10). Again, it is evident from the capacitance data (Table 3) that all of the films containing nc-ATO display a marked increase in surface charge density. It is also apparent that the series resistances of all of the films containing nc-ATO are much lower than those containing just  $\alpha\text{-Fe}_2\text{O}_3$ , even when hematite is deposited on top of the nc-ATO 2D and 3D structures. In addition, the films containing only hematite in either 2D or 3D morphologies display nearly identical capacitance values to each other as well as to the bare FTO substrate. From these observations, a number of conclusions can be drawn regarding the charge transport processes occurring within the semiconductor materials. First, and most importantly, since these measurements were taken in a region of non-Faradaic activity, then necessarily the capacitance values measured at 1.00 V are not representative of the active surface areas of the films, but rather are representative of the relative polarizations of the films, due to charge buildup in the space-charge region. Again, an accurate comparison can be achieved by looking at the ratios of capacitances for different morphologies of the same semiconductor material, as discussed above, but only to determine electronically accessible surface area (not active surface states). Second, all of the films containing nc-ATO have lower series resistances, similar to the bare FTO electrode, which is again an expected result

**TABLE 3. Net Relative Capacitance Values ( $C_N$ ) and Series and Charge Transfer Resistances (in Ohms) Determined for All Films at the Two Applied Potentials Listed<sup>a</sup>**

$V_{app}$		FTO only (A)	nc-ATO 2D (B)	nc-ATO 3D (C)	Fe <sub>2</sub> O <sub>3</sub> 2D (D)	Fe <sub>2</sub> O <sub>3</sub> 3D (E)	Fe <sub>2</sub> O <sub>3</sub> on nc-ATO 2D (F)	Fe <sub>2</sub> O <sub>3</sub> on nc-ATO 3D (G)
1.00 V	$R_{ct}$				$+5 \times 10^5$		$*2.5 \times 10^5$	$*5.8 \times 10^4$
	$C_N$ (rel)	<b>1.000</b>	<b>12.95</b>	<b>217.5</b>	<b>1.13</b>	<b>1.14</b>	<b>13.90</b>	<b>136.0</b>
	$R_s$	*24	25.54	14.58	+160	1020	30.2	13.120
1.65 V	$R_{ct}$	2152	9800	*4700	82	119.4	37.1	6.97
	$C_N$ (rel)	<b>1.000</b>	<b>6.66</b>	<b>143.3</b>	<b>54</b>	<b>13.5</b>	<b>95</b>	<b>677</b>
	$R_s$	8.54	36.3	8.73	42.5	25.1	24.4	10.88

<sup>a</sup> All values have associated errors below 5%, with the exception of the values marked with \* that have associated errors of 10% or less, and the values marked with + that have associated errors of 25% or less. For the charge transfer resistances at 1.00 V, the charge passed across the SCLJ can be assumed to be negligible. These resistances could not be accurately measured from the fitting process and are therefore assumed (for all intents and purposes herein) to be infinite.

given the excellent charge transport capabilities of the transparent conducting oxides. Conversely, the films containing only hematite (2D and 3D) demonstrated much higher series resistances and capacitance values on par with the bare electrode. This is again consistent with the analysis of Figure 3 and Table 1, in that the electrochemically accessible surface area of the  $\alpha$ -Fe<sub>2</sub>O<sub>3</sub> is localized close to the FTO surface.

Finally, when considering nc-ATO films with and without iron oxide deposited on the surface, the capacitance values tend to be quite consistent. The planar films containing nc-ATO (curves B and F) have nearly identical capacitance values. A similar observation is made for the 3D films containing nc-ATO (curves C and G), which demonstrate comparable capacitances, as well. The most likely reason for this is facile infiltration of electrolyte into the porous structure, which has been confirmed by initial ellipsometric porosimetry measurements (data not given).

Upon evaluation of the capacitances at a higher applied potential of 1.65 V, the capacitance values of the films containing  $\alpha$ -Fe<sub>2</sub>O<sub>3</sub> increased substantially with respect to the bare FTO electrode. Recent works by Klahr *et al.*<sup>32,36</sup> and by Cummings *et al.*<sup>27,28</sup> have suggested that surface states, which can act as recombination centers, are active in the oxidation of water and glucose (these have tentatively been assigned as Fe(IV) surface species). As discussed in Klahr's works, the contribution of these states to the equivalent circuit diagram for water oxidation can be represented by a capacitor in parallel with a second capacitor that accounts for "bulk" contributions to the overall storage of charge by the material, in this case due to the space-charge region and the electrical double layer at the semiconductor surface. However, when presented with only one semicircle in the Nyquist plot in the dark, a Randles' equivalent circuit is necessarily warranted. Cummings *et al.* similarly demonstrated the use of a parallel RC circuit when evaluating the impedance response in the low-frequency regime, as is the case here, and assumed that the pseudocapacitance resulting from these surface states greatly outweighed the capacitance from the space-charge region of the

hematite film. We therefore necessarily impose the same assumptions here such that any ratio of capacitances measured at 1.65 V applied potential for films containing hematite is a ratio of the number of catalytically active species on the surface of the catalyst.

The important point to note is the substantial increase in the number of active surface states available to the hematite layer deposited onto the walls of the 3D nc-ATO macroporous structure. This film demonstrated an approximately 7-fold increase in surface area with respect to its 2D planar counterpart (see Table 3) at an applied potential of 1.65 V vs RHE, which is of course a result of the high surface area 3D support. Not only is this surface area enhancement useful in water-splitting applications, but it could also be of great benefit in supercapacitor applications, where hematite nanostructures are showing great promise as cheap and efficient charge storage materials, and for which high capacitances are desired.<sup>52–54</sup>

A number of other interesting properties can be elucidated from the data in Table 3. First, attention is drawn to the 2D and 3D films containing hematite only. At 1.00 V, the two films show near-identical capacitance values, in agreement with the values in Table 1. However, at a higher potential of 1.65 V, the 2D film shows a marked increase in available surface recombination centers compared to the 3D film, again consistent with the above discussion and the results of the voltammograms presented in Figure 2a.

Second, upon increasing the potential from 1.00 to 1.65 V, the capacitance of the 2D and 3D nc-ATO films actually *decreases* with respect to the bare FTO electrode. This is likely a result of the higher overpotential required by the nc-ATO films to initiate the water-splitting reaction. From the Tafel plots in Figure 4 and the voltammograms in Figure 2b, it is evident that the nc-ATO 2D and 3D films require a higher applied potential before they can begin water oxidation. The Tafel slope extrapolated for the bare FTO substrate (see Table 2) is slightly lower than the slopes for the two nc-ATO films. It is therefore probable that, at 1.65 V applied potential, the bare FTO electrode demonstrates better kinetics toward the water oxidation reaction,

which is also evident from the lower charge transfer resistance it displays in Table 3.

**Electronic Effects on Film Activity.** One of the most interesting results from the data in Table 3 is the comparison between the charge transfer resistances determined for the hematite films in the presence and absence of nc-ATO. In both 2D and 3D cases, the charge transfer resistances are lower for the films that contain “underlayers” or 2D and 3D support structures of nc-ATO (curves F and G), as compared to the 2D and 3D morphologies of  $\alpha$ -Fe<sub>2</sub>O<sub>3</sub> deposited directly onto the FTO substrates (curves D and E). Specifically, the 2D films in both cases (with and without a 2D nc-ATO underlayer film) show similar surface roughness values from the AFM measurements where in fact the surface roughness of the  $\alpha$ -Fe<sub>2</sub>O<sub>3</sub>-nc-ATO bilayer film is *lower* than the surface roughness of the pure hematite film (Figures S6 and S7). Yet despite this, and despite the same thickness of hematite deposited on both films (with and without nc-ATO), the activity of the  $\alpha$ -Fe<sub>2</sub>O<sub>3</sub> film deposited on top of the nc-ATO 2D film shows a marked increase in electrochemically active surface area, as well as a decrease in charge transfer resistance and overpotential (from Table 3 and Figure 2a, respectively). Given the nature of the construction of the films, it is possible that, for the case where nc-ATO is present between the FTO substrate and the hematite overlayer, the nc-ATO acts as an electronic “spacer” between the  $\alpha$ -Fe<sub>2</sub>O<sub>3</sub> and the FTO glass. Since the FTO substrate is connected to the leads of the potentiostat, it acts as an electron “sink” for the film. When nc-ATO is present and serves to inject electrons from the SCLJ into the FTO glass, it effectively decreases the probability of interaction of these electrons with the catalytically active sites/intermediates on the surface of the hematite material, therefore increasing the current density and capacitance, while decreasing the charge transfer resistance through the film system. The same conclusion was recently made by Hisatomi *et al.*, where they found that underlayers of Nb<sub>2</sub>O<sub>5</sub> and TiO<sub>2</sub> helped to dramatically suppress charge recombination between injected electrons in the FTO substrate and surface holes on the overlying ultrathin hematite photocatalyst, both under light and dark conditions.<sup>19</sup> We can therefore conclude that underlayers play a very important role in PEC applications and should be investigated further in order to more precisely elucidate their beneficial properties. Theoretical studies on the effect of surface species on the catalytic activity of hematite could be used in conjunction with investigations into “underlayer” structures in order to determine whether the enhanced activity is the result of kinetic or thermodynamic effects (or a combination of the two), and whether in the latter case the free energy of binding of intermediates to the surface is affected by the presence of an underlayer structure.<sup>39,49</sup> Combined with surface state modification and doping, these bilayer

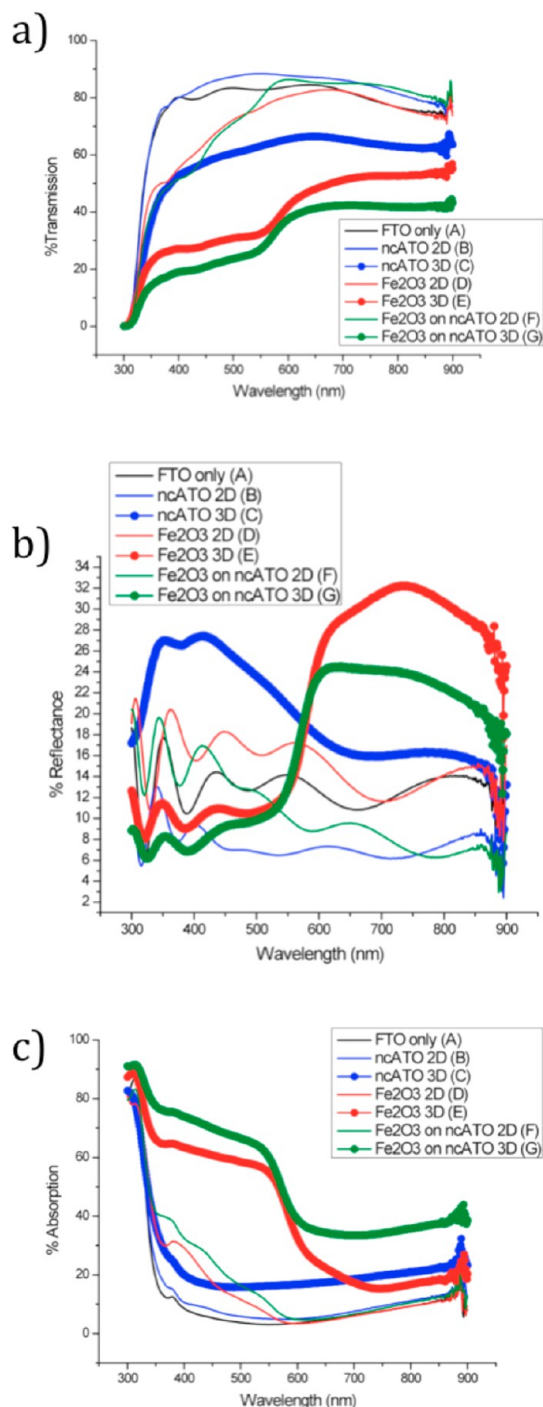


**Figure 6.** (a) Transmission, (b) reflectance, and (c) absorption measurements of all seven films tested in this study. The transmission and reflectance measurements were performed at the front and back of the integrating sphere, respectively, and were used to estimate the percent of light absorbed by the films as a function of wavelength.

structures could prove to be very efficient water-splitting catalysts for (photo)electrochemical applications.<sup>55</sup>

In addition to the above, XPS measurements were taken on the 2D nc-ATO and  $\alpha$ -Fe<sub>2</sub>O<sub>3</sub> individual films in order to determine the energy band alignment between the two materials and to further investigate the

reason for the enhanced activity of the hematite/nc-ATO bilayer film (see Figures S4 and S11). From the energy band diagram in Figure S11, it is clear that there is a beneficial alignment between the  $\alpha$ -Fe<sub>2</sub>O<sub>3</sub>, the nc-ATO, and the FTO glass. Although this is less of a concern in the present case (dark electrolysis of water), and given the fact that charge transport likely occurs primarily through a hopping mechanism across the surface of the hematite material,<sup>27</sup> this band alignment may prove to be of great benefit for future photoelectrochemical measurements using the same film construction and morphology.<sup>13</sup>

**UV–Vis Measurements: Absorption, Transmission, and Reflection.** Considering the disordered nature of the macroporous inverse opal structures, concern over the absorption and scattering properties of the films for photoelectrochemical applications warranted an investigation into the absorption, transmission, and reflection of UV/visible light by the materials. Figure 6 shows the transmission, reflection, and absorption measurements for all of the films prepared in this study from 300 to 900 nm. It is clear from these data that light scattering by the films is not problematic within the range of absorption of the material. Specifically, for macroporous films containing hematite (the  $\alpha$ -Fe<sub>2</sub>O<sub>3</sub> on a 3D nc-ATO support and the pure 3D  $\alpha$ -Fe<sub>2</sub>O<sub>3</sub> film), a strong reflectance is observed, but only for photons with wavelengths greater than the absorption edge of the  $\alpha$ -Fe<sub>2</sub>O<sub>3</sub>, around 600 nm. For the spectral region in the vicinity of 300 to 600 nm, reflectance decreases substantially, even below the level of the transparent 2D films containing hematite, and absorption increases dramatically, as shown in Figure 6c. This increase in absorption is a result of the much greater amount of hematite that can be deposited as a structured 3D film, or onto a 3D structured film, over the same geometric or “apparent” surface area. Furthermore, previous literature reports suggest that disordered inverse opal structures may also help to increase the path length of light within their disordered structure.<sup>26</sup> This property is extremely important in the evaluation of the photoelectrochemical properties of these films, which are currently under investigation in our lab, and the use of disordered macroporous inverse opal 3D electrodes in photoelectrochemical systems.

## CONCLUSION

We have demonstrated an example of a 3D nc-ATO disordered macroporous inverse opal electrode as an

efficient high surface area support for the electrochemical splitting of water using hematite. Cyclic voltammetry was employed in order to demonstrate the high current outputs achievable by use of these 3D macroporous transparent conducting oxide supports. Electrochemical models and macroscopic kinetic theories were employed in order to evaluate the surface area enhancement achieved by using 2D and 3D films of nc-ATO. The non-Faradaic region of the CV spectra was modeled using a simple RC circuit, which was later correlated to EIS measurements in the same region, and the Faradaic portion of the CV was evaluated using the Tafel relation, in order to distinguish between electronic and geometric contributions to activity enhancement between various films and to assess mechanistic aspects of the water oxidation reaction at the catalyst surfaces. Electrochemical impedance spectroscopy was used to evaluate the capacitance and charge transfer properties of the films and was found to agree well with the exponential decay model (RC circuit) applied to the cyclic voltammograms. The enhanced surface area resulting from the use of a 3D nc-ATO support structure was quantified by the increased number of catalytically active sites on the surface of the hematite catalysts. Charge transfer resistances were also found to be substantially lower for films containing hematite, as expected given the better kinetic activity of the  $\alpha$ -Fe<sub>2</sub>O<sub>3</sub> films compared to the nc-ATO and FTO samples, and as evidenced by the low output currents in the cyclic voltammograms associated with these transparent conducting oxides. Additionally, it was suggested that lower charge transfer resistances and increased surface area (capacitance) of the films with nc-ATO underlayers could be a result of the film construction which allows for effective removal and separation of electrons from the SCLJ, hence decreasing the rate of recombination with surface trap states. Finally, absorption, transmission, and reflectance measurements were performed on all of the tested films and demonstrated that the disordered macroporous 3D films absorbed a substantial portion of light above the band gap of hematite, even more so than the 2D planar films of hematite, suggesting that not only is a greater absorption of light possible for a 3D inverse opal structure than for a 2D film of the same geometric (apparent) surface area, but this property could be of extreme value in photoelectrochemical systems that would also benefit from the efficient charge transfer and high electrochemical surface areas provided by the 3D electrodes described here.

## METHODS

All reagents and solvents were used as received without further purification. Iron(III) nitrate nonahydrate, antimony(III) ethoxide, and tin(IV) chloride were purchased from Aldrich. Benzyl alcohol was purchased from Acros; 30% hydrogen peroxide solution was purchased from Caledon; sulfuric acid was purchased from Fisher Scientific; and sodium hydroxide

and 28% ammonium hydroxide solution were purchased from ACP. Fluorine-doped tin oxide (FTO) glass slides were purchased from Hartford Glass Inc.; these substrates were pretreated overnight in a 3:1 mixture of NH<sub>4</sub>OH/H<sub>2</sub>O<sub>2</sub>, rinsed with 18.3 $\Omega$  deionized water, and stored in ethanol. Silicon wafers were purchased from Wafer World and were similarly pretreated overnight in a 3:1 mixture of H<sub>2</sub>SO<sub>4</sub>/H<sub>2</sub>O<sub>2</sub>, rinsed with deionized



water, and stored in ethanol. Before film deposition, each FTO (and silicon) substrate was plasma-treated in an SPI Supplies Plasma Prep III solid-state plasma cleaner for at least 5 min under low-pressure  $O_2$  atmosphere. In all cases, when depositing precursor materials onto the FTO substrates, a small part of the glass electrode was covered by 3 M transparent tape to later allow for connection to the electrochemical equipment. All films had approximately the same geometric (apparent) surface area of  $6\text{ cm}^2$ .

Cyclic voltammetry (CV) and electrochemical impedance spectroscopy (EIS) measurements were performed using a Solartron SI 1287 electrochemical interface instrument coupled to a Solartron SI 1260 impedance/gain-phase analyzer. Measurements were taken in a standard three-electrode setup using the sample film on FTO as the working electrode, platinum wire as the counter electrode, and a Hg/HgO reference electrode (Koslow Scientific Company, 5088). Cyclic voltammetry scans were performed in the dark in 1.0 M NaOH at a scan rate of 0.020 V/s. The system was scanned from 0 to 1.1 V vs Hg/HgO and was cycled several times before being evaluated. The non-Faradaic potential regions of the cyclic voltammograms in Figure 3 were modeled according to the procedure in the Supporting Information. Impedance measurements were performed at applied potentials of 0.100 and 0.750 vs Hg/HgO ( $\sim 1.00$  and  $1.65\text{ V}$  vs RHE, respectively) in the same electrolyte under dark conditions, within a cycling range of  $\pm 10\text{ mV}$  and cycled at frequencies of  $\sim 7000$  to  $0.1\text{ Hz}$ . The data were acquired using Zplot software and were fitted using a Randles' equivalent circuit shown in Figure 5 using Zview software, with a constant phase element (CPE) replacing the capacitor in the equivalent circuit. Resistances and capacitance values are displayed in Table 3 with the CPE exponential terms determined from the fitting displayed in Table S1 in the Supporting Information. X-ray diffraction (XRD) spectra were acquired using a Siemens 55000 diffractometer with a  $Cu\ K\alpha$  X-ray source at a scan rate of  $0.027^\circ/\text{s}$  and over a range of  $20$ – $62\ 2\theta$  for the  $Fe_2O_3$  and nc-ATO samples and at a scan rate of  $0.013^\circ/\text{s}$  and over a range of  $10$ – $60\ 2\theta$  for the  $Fe_2O_3$  on nc-ATO composite sample (see Supporting Information). Scanning electron microscope (SEM) images were taken using a Hitachi S-5200 scanning electron microscope at the voltage and magnification specified in each image. Atomic force microscopy (AFM) measurements were performed using an atomic force microscope from Digital Instruments (Dimension 5000) operated in tapping mode to examine the surface topography and determine the roughness. A rectangular-shaped silicon probe (NanoWorld, NCH) with a resonance frequency of  $320\text{ kHz}$  and a spring constant of  $42\text{ N/m}$  was used. Spectroscopic ellipsometry measurements were performed using a Sopra GES-5E ellipsometer at a fixed incident angle of  $75^\circ$  and scanned between  $1.2$  and  $4\text{ eV}$ . Spectra were then analyzed and fitted using Winelli software provided by the manufacturer (spectra not included). X-ray photoelectron spectroscopy measurements were performed using a PHI 5500 MultiTechnique system. Absorption, transmission, and reflectance spectra were measured as a percent of the total number of photons. The percentage of photons absorbed by each sample was estimated using the equation  $\%A = 100 - (\%T + \%R)$ , where  $\%T$  and  $\%R$  are the percentage of spectral and diffuse light transmitted and reflected by the sample, respectively. The  $\%T$  and  $\%R$  values were measured using an integrating sphere accessory in a UV/vis/NIR spectrometer (Perkin-Elmer Lambda 1050).

**Synthesis of Polystyrene Spheres.** The polystyrene opals were synthesized according to a modified literature procedure.<sup>56</sup> Briefly, styrene monomer ( $262\text{ mmol}$ ,  $30\text{ mL}$ ) was added to  $200\text{ mL}$  of deionized water in a  $500\text{ mL}$  three-neck round-bottom flask equipped with a mechanical stirrer (glass rod with a Teflon blade), a reflux condenser, and a nitrogen purge. The flask was brought to  $72^\circ\text{C}$ , and nitrogen was bubbled through the solution for  $10\text{ min}$ , at which point potassium persulfate ( $322\text{ mg}$ ,  $1.19\text{ mmol}$ ) in  $10\text{ mL}$  of water was added all at once to the flask. The mixture was allowed to stir for  $24\text{ h}$  at  $72^\circ\text{C}$ , at which point it was slowly allowed to cool to room temperature. Following this, the white cloudy mixture was diluted to 200% its volume with ethanol and centrifuged for  $10\text{ min}$  at  $\sim 7000\text{ rpm}$ . The solvent was decanted off, and the resulting  $550\text{ nm}$

polystyrene opals were redispersed in ethanol to a concentration of  $\sim 0.16\text{ g/mL}$  (see Supporting Information for SEM images).

**Preparation of the Precursor Solutions.** The iron precursor was prepared by adding  $9\text{ g}$  of  $Fe(NO_3)_3 \cdot 9H_2O$  to  $80\text{ mL}$  of ethanol and  $20\text{ mL}$  of deionized water.<sup>57</sup> The reaction mixture was allowed to stir at room temperature for at least  $24\text{ h}$  and was then filtered through  $0.7\text{ }\mu\text{m}$  syringe filters, yielding a  $0.016\text{ g/mL}$  clear, orange liquid. The antimony-doped tin oxide nanocrystals were synthesized according to a previous literature procedure, yielding a  $0.05\text{ g/mL}$  dispersion of nc-ATO.<sup>25</sup>

**Preparation of Thin Films (2D Samples) of  $Fe_2O_3$  and nc-ATO.** Films of  $Fe_2O_3$  and nc-ATO were prepared via spin-coating of the respective precursor dispersions/solutions onto FTO glass substrates (thicknesses were determined via ellipsometry and SEM cross-section analyses). Solutions were spun at  $3000\text{ rpm}$  for  $30\text{ s}$  at an acceleration of  $3990\text{ rpm/s}$  (a small section of the FTO glass was blocked using 3M transparent tape to later allow connection to the electrochemical instruments). The films were then annealed at  $450^\circ\text{C}$  for a minimum of  $16\text{ h}$ , yielding  $\sim 80\text{ nm}$  thick films of nc-ATO and  $\sim 20\text{ nm}$  thick films of  $\alpha\text{-Fe}_2\text{O}_3$ . The  $\alpha\text{-Fe}_2\text{O}_3$ /nc-ATO bilayer was produced by subsequent spin-coating and annealing of each of the precursor dispersions/solutions using the above procedure (see Figure 1d,e).

**Preparation of nc-ATO Macroporous Films (3D Samples).** The polystyrene spheres were doctor-bladed onto FTO glass substrates (a small section of the FTO glass was again blocked using 3M transparent tape to later allow connection to the electrochemical instruments). Following this, the spheres were necked at  $78^\circ\text{C}$  for at least  $16\text{ h}$ , and the nc-ATO precursor dispersion was spin-coated ( $1500\text{ rpm}$ ,  $3990\text{ rpm/s}$  for  $30\text{ s}$ ) onto the films of polystyrene opals to allow for infiltration between the spheres, and then heated at  $78^\circ\text{C}$  for  $10\text{ min}$  to remove residual solvent. This spin-coating/heating process was repeated an additional three times to ensure appropriate infiltration of the nc-ATO. The films were then heated at  $450^\circ\text{C}$  for at least  $16\text{ h}$  to anneal the films and remove the polystyrene spheres, yielding a 3D nc-ATO macroporous (inverse opal) structure.

**Preparation of  $Fe_2O_3$  Macroporous and  $Fe_2O_3$  on nc-ATO Macroporous Films (3D Samples).**  $Fe_2O_3$  inverse opals were prepared by doctor-blading the  $550\text{ nm}$  polystyrene spheres onto FTO glass substrates. Following this, the spheres were necked at  $78^\circ\text{C}$  for a minimum of  $16\text{ h}$ , and the  $Fe_2O_3$  precursor solution was wet impregnated onto the films to allow infiltration between the polystyrene opals. The films were then heated at  $78^\circ\text{C}$  for  $10\text{ min}$ , then annealed at  $450^\circ\text{C}$  for at least  $16\text{ h}$ . The same procedure was followed for depositing  $Fe_2O_3$  onto the nc-ATO macroporous structure prepared above (wet impregnated into the structure, heated for  $10\text{ min}$  at  $78^\circ\text{C}$ , and annealed at  $450^\circ\text{C}$  for at least  $16\text{ h}$ ).

**Conflict of Interest:** The authors declare no competing financial interest.

**Acknowledgment.** G.A.O. is Government of Canada Research Chair in Materials Chemistry and Nanochemistry. He is deeply indebted to the Natural Sciences and Engineering Research Council of Canada and to MRI-UoT for research funding. J.M. would like to thank the University of Toronto for the University of Toronto Fellowship, and Dalton Pharma Services for the DPS Advanced Inorganic and Materials Laboratory Fellowship. The authors would like to thank Dr. Neil Coombs and Ilya Gourevich for technical help in SEM imaging, Professor Gilbert Walker for use of his AFM instrumentation, and Laura Hoch for helpful suggestions and editorial comments.

**Supporting Information Available:** Additional SEM images, Tafel plots, XRD spectra, AFM images, XPS spectra, and additional Nyquist plots, as well as an energy band alignment diagram and derivation of some equations. This material is available free of charge via the Internet at <http://pubs.acs.org>.

## REFERENCES AND NOTES

1. Riha, S. C.; Devries Vermeer, M. J.; Pellin, M. J.; Hupp, J. T.; Martinson, A. B. F. Hematite-Based Photo-oxidation of Water Using Transparent Distributed Current Collectors. *ACS Appl. Mater. Interfaces* **2013**, *5*, 360–367.



2. Kamegawa, T.; Suzuki, N.; Yamashita, H. Design of Macroporous TiO<sub>2</sub> Thin Film Photocatalysts with Enhanced Photofunctional Properties. *Energy Environ. Sci.* **2011**, *4*, 1411.
3. Lin, Y.; Zhou, S.; Sheehan, S. W.; Wang, D. Nanonet-Based Hematite Heteronanostructures for Efficient Solar Water Splitting. *J. Am. Chem. Soc.* **2011**, *133*, 2398–2401.
4. Boettcher, S. W.; Warren, E. L.; Putnam, M. C.; Santori, E. A.; Turner-Evans, D.; Kelzenberg, M. D.; Walter, M. G.; McKone, J. R.; Brunschwig, B. S.; Atwater, H. A.; et al. Photoelectrochemical Hydrogen Evolution Using Si Microwire Arrays. *J. Am. Chem. Soc.* **2011**, *133*, 1216–1219.
5. Zeng, K.; Zhang, D. Recent Progress in Alkaline Water Electrolysis for Hydrogen Production and Applications. *Prog. Energy Combust. Sci.* **2010**, *36*, 307–326.
6. Dau, H.; Limberg, C.; Reier, T.; Risch, M.; Roggan, S.; Strasser, P. The Mechanism of Water Oxidation: From Electrolysis via Homogeneous to Biological Catalysis. *ChemCatChem* **2010**, *2*, 724–761.
7. Sivula, K.; Zboril, R.; Le Formal, F.; Robert, R.; Weidenkaff, A.; Tucek, J.; Frydrych, J.; Grätzel, M. Photoelectrochemical Water Splitting with Mesoporous Hematite Prepared by a Solution-Based Colloidal Approach. *J. Am. Chem. Soc.* **2010**, *132*, 7436–7444.
8. Nocera, D. G. The Artificial Leaf. *Acc. Chem. Res.* **2012**, *45*, 767–776.
9. Fujishima, A.; Honda, K. Electrochemical Photolysis of Water at a Semiconductor Electrode. *Nature* **1972**, *238*, 37–38.
10. Kay, A.; Cesar, I.; Grätzel, M. New Benchmark for Water Photooxidation by Nanostructured  $\alpha$ -Fe<sub>2</sub>O<sub>3</sub> Films. *J. Am. Chem. Soc.* **2006**, *128*, 15714–15721.
11. Hou, Y.; Zuo, F.; Dagg, A.; Feng, P. A Three-Dimensional Branched Cobalt-Doped  $\alpha$ -Fe<sub>2</sub>O<sub>3</sub> Nanorod/MgFe<sub>2</sub>O<sub>4</sub> Heterojunction Array as a Flexible Photoanode for Efficient Photoelectrochemical Water Oxidation. *Angew. Chem., Int. Ed.* **2013**, *125*, 1286–1290.
12. Zhang, L.; Baumanis, C.; Robben, L.; Kandiel, T.; Bahnemann, D. Bi<sub>2</sub>WO<sub>6</sub> Inverse Opals: Facile Fabrication and Efficient Visible-Light-Driven Photocatalytic and Photoelectrochemical Water-Splitting Activity. *Small* **2011**, *7*, 2714–2720.
13. Sivula, K.; Le Formal, F.; Grätzel, M. WO<sub>3</sub>–Fe<sub>2</sub>O<sub>3</sub> Photoanodes for Water Splitting: A Host Scaffold, Guest Absorber Approach. *Chem. Mater.* **2009**, *21*, 2862–2867.
14. Sordello, F.; Maurino, V.; Minero, C. Photoelectrochemical Study of TiO<sub>2</sub> Inverse Opals. *J. Mater. Chem.* **2011**, *21*, 19144–19152.
15. Huang, Y.-J.; Lai, C.-H.; Wu, P.-W.; Chen, L.-Y. Ni Inverse Opals for Water Electrolysis in an Alkaline Electrolyte. *J. Electrochem. Soc.* **2010**, *157*, P18–P22.
16. Chen, X.; Ye, J.; Ouyang, S.; Kako, T.; Li, Z.; Zou, Z. Enhanced Incident Photon-to-Electron Conversion Efficiency of Tungsten Trioxide Photoanodes Based on 3D-Photonic Crystal Design. *ACS Nano* **2011**, *5*, 4310–4318.
17. Yang, Z.; Gao, S.; Li, W.; Vlasko-Vlasov, V.; Welp, U.; Kwok, W.-K.; Xu, T. Three-Dimensional Photonic Crystal Fluorinated Tin Oxide (FTO) Electrodes: Synthesis and Optical and Electrical Properties. *ACS Appl. Mater. Interfaces* **2011**, *3*, 1101–1108.
18. Gaillot, D. P.; Summers, C. J. Inverse Opal Photonics. In *Atomic Layer Deposition of Nanostructured Materials*; Wiley-VCH Verlag GmbH: Weinheim, Germany, 2012; pp 345–376.
19. Hisatomi, T.; Dotan, H.; Stefiak, M.; Sivula, K.; Rothschild, A.; Grätzel, M.; Mathews, N. Enhancement in the Performance of Ultrathin Hematite Photoanode for Water Splitting by an Oxide Underlayer. *Adv. Mater.* **2012**, *24*, 2699–2702.
20. Duret, A.; Grätzel, M. Visible Light-Induced Water Oxidation on Mesoscopic  $\alpha$ -Fe<sub>2</sub>O<sub>3</sub> Films Made by Ultrasonic Spray Pyrolysis. *J. Phys. Chem. B* **2005**, *109*, 17184–17191.
21. Xi, L.; Bassi, P. S.; Chiam, S. Y.; Mak, W. F.; Tran, P. D.; Barber, J.; Chye Loo, J. S.; Wong, L. H. Surface Treatment of Hematite Photoanodes with Zinc Acetate for Water Oxidation. *Nanoscale* **2012**, *4*, 4430–4433.
22. Cornuz, M.; Grätzel, M.; Sivula, K. Preferential Orientation in Hematite Films for Solar Hydrogen Production via Water Splitting. *Chem. Vap. Deposition* **2010**, *16*, 291–295.
23. Schreiber, R. S.; Ballesteros, L.; Burgos, A.; Munoz, E. C.; Grez, P.; Leinen, D.; Martín, F.; Ramón Ramos-Barrado, J.; Dalchiele, E. A. Electrodeposited Nanostructured  $\alpha$ -Fe<sub>2</sub>O<sub>3</sub> Photoanodes for Solar Water Splitting: Effect of Surface Co-modification on Photoelectrochemical Performance. *J. Electrochem. Soc.* **2011**, *158*, D500–D505.
24. Arsenault, E.; Soheilnia, N.; Ozin, G. A. Periodic Macroporous Nanocrystalline Antimony-Doped Tin Oxide Electrode. *ACS Nano* **2011**, *5*, 2984–2988.
25. Müller, V.; Rasp, M.; Stefanic, G.; Ba, J.; Günther, S.; Rathousky, J.; Niederberger, M.; Fattakhova-Rohlfing, D. Highly Conducting Nanosized Monodispersed Antimony-Doped Tin Oxide Particles Synthesized via Nonaqueous Sol–Gel Procedure. *Chem. Mater.* **2009**, *21*, 5229–5236.
26. Neale, N. R.; Lee, B. G.; Kang, S. H.; Frank, A. J. Near-Infrared Light Trapping in Disordered Inverse Opals. *J. Phys. Chem. C* **2011**, *115*, 14341–14346.
27. Cummings, C. Y.; Marken, F.; Peter, L. M.; Wijayantha, K. G. U.; Tahir, A. A. New Insights into Water Splitting at Mesoporous  $\alpha$ -Fe<sub>2</sub>O<sub>3</sub> Films: A Study by Modulated Transmittance and Impedance Spectroscopies. *J. Am. Chem. Soc.* **2012**, *134*, 1228–1234.
28. Cummings, C. Y.; Bonné, M. J.; Edler, K. J.; Helton, M.; McKee, A.; Marken, F. Direct Reversible Voltammetry and Electrocatalysis with Surface-Stabilised Fe<sub>2</sub>O<sub>3</sub> Redox States. *Electrochem. Commun.* **2008**, *10*, 1773–1776.
29. Yeo, R. S.; Orehotzky, J.; Visscher, W.; Srinivasan, S. Ruthenium-Based Mixed Oxides as Electrocatalysts for Oxygen Evolution in Acid Electrolytes. *J. Electrochem. Soc.* **1981**, *128*, 1900–1904.
30. Bard, A. J.; Faulkner, L. R. *Electrochemical Methods: Fundamentals and Applications*, 2nd ed.; John Wiley and Sons, Inc.: Danvers, MA, 2001; Vol. 38, pp 12–16.
31. Hens, Z. The Electrochemical Impedance of One-Equivalent Electrode Processes at Dark Semiconductor/Redox Electrodes Involving Charge Transfer through Surface States. 1. Theory. *J. Phys. Chem. B* **1999**, *103*, 122–129.
32. Klahr, B.; Gimenez, S.; Fabregat-Santiago, F.; Hamann, T.; Bisquert, J. Water Oxidation at Hematite Photoelectrodes: The Role of Surface States. *J. Am. Chem. Soc.* **2012**, *134*, 4294–4302.
33. Rajeshwar, K. Fundamentals of Semiconductor Electrochemistry and Photoelectrochemistry. *Encycl. Electrochem.* **2007**, 1–51.
34. Bott, A. W. Electrochemistry of Semiconductors. *Curr. Sep.* **1998**, *17*, 87–91.
35. Zhang, Z.; Yates, J. T. Band Bending in Semiconductors: Chemical and Physical Consequences at Surfaces and Interfaces. *Chem. Rev.* **2012**, *112*, 5520–5551.
36. Klahr, B.; Gimenez, S.; Fabregat-Santiago, F.; Bisquert, J.; Hamann, T. W. Electrochemical and Photoelectrochemical Investigation of Water Oxidation with Hematite Electrodes. *Energy Environ. Sci.* **2012**, *5*, 7626–7636.
37. Bard, A. J.; Faulkner, L. R. *Electrochemical Methods: Fundamentals and Applications*; John Wiley and Sons, Inc.: Danvers, MA, 2001; pp 87–115.
38. Walter, M. G.; Warren, E. L.; McKone, J. R.; Boettcher, S. W.; Mi, Q.; Santori, E. A.; Lewis, N. S. Solar Water Splitting Cells. *Chem. Rev.* **2010**, *110*, 6446–6473.
39. Fang, Y.-H.; Liu, Z.-P. Mechanism and Tafel Lines of Electrooxidation of Water to Oxygen on RuO<sub>2</sub>(110). *J. Am. Chem. Soc.* **2010**, *132*, 18214–18222.
40. Seley, D.; Ayers, K.; Parkinson, B. A. Combinatorial Search for Improved Metal Oxide Oxygen Evolution Electrocatalysts in Acidic Electrolytes. *ACS Comb. Sci.* **2013**, *15*, 82–89.
41. Guerrini, E.; Chen, H.; Trasatti, S. Oxygen Evolution on Aged IrO<sub>x</sub>/Ti Electrodes in Alkaline Solutions. *J. Solid State Electrochem.* **2006**, *11*, 939–945.
42. Fletcher, S. Tafel Slopes from First Principles. *J. Solid State Electrochem.* **2009**, *13*, 537–549.

43. Bauer, H. H. The Electrochemical Transfer-Coefficient. *J. Electroanal. Chem. Interfacial Electrochem.* **1968**, *16*, 419–432.
44. Mustain, W. E.; Prakash, J. Kinetics and Mechanism for the Oxygen Reduction Reaction on Polycrystalline Cobalt–Palladium Electrocatalysts in Acid Media. *J. Power Sources* **2007**, *170*, 28–37.
45. Fiori, G.; Mari, C. Electrocatalysis of Oxygen Evolution. *Int. J. Hydrogen Energy* **1982**, *7*, 489–493.
46. Castro, E. B.; Gervasi, C. A. Electrodeposited Ni–Co-Oxide Electrodes: Characterization and Kinetics of the Oxygen Evolution Reaction. *Int. J. Hydrogen Energy* **2000**, *25*, 1163–1170.
47. Gerken, J. B.; McAlpin, J. G.; Chen, J. Y. C.; Rigsby, M. L.; Casey, W. H.; Britt, R. D.; Stahl, S. S. Electrochemical Water Oxidation with Cobalt-Based Electrocatalysts from pH 0–14: The Thermodynamic Basis for Catalyst Structure, Stability, and Activity. *J. Am. Chem. Soc.* **2011**, *133*, 14431–14442.
48. Koza, J. A.; He, Z.; Miller, A. S.; Switzer, J. A. Electrodeposition of Crystalline  $\text{Co}_3\text{O}_4$ —A Catalyst for the Oxygen Evolution Reaction. *Chem. Mater.* **2012**, *24*, 3567–3573.
49. Koper, M. T. M. Thermodynamic Theory of Multi-electron Transfer Reactions: Implications for Electrocatalysis. *J. Electroanal. Chem.* **2011**, *660*, 254–260.
50. De Pauli, C. P.; Trasatti, S. Composite Materials for Electrocatalysis of  $\text{O}_2$  Evolution:  $\text{IrO}_2+\text{SnO}_2$  in Acid Solution. *J. Electroanal. Chem.* **2002**, *538–539*, 145–151.
51. Lvovich, V. F. Equivalent Circuits Modeling of the Impedance Phenomenon. In *Impedance Spectroscopy: Applications to Electrochemical and Dielectric Phenomena*; John Wiley and Sons, Inc.: New York, 2012; pp 37–47.
52. Bora, D. K.; Braun, A.; Constable, E. C. “In Rust We Trust”. Hematite—The Prospective Inorganic Backbone for Artificial Photosynthesis. *Energy Environ. Sci.* **2013**, *6*, 407–425.
53. Sun, B.; Horvat, J.; Kim, H. S.; Kim, W.; Ahn, J.; Wang, G. Synthesis of Mesoporous  $\alpha\text{-Fe}_2\text{O}_3$  Nanostructures for Highly Sensitive Gas Sensors and High Capacity Anode Materials in Lithium Ion Batteries. *J. Phys. Chem. C* **2010**, *114*, 18753–18761.
54. Zhu, M.; Wang, Y.; Meng, D.; Qin, X.; Diao, G. Hydrothermal Synthesis of Hematite Nanoparticles and Their Electrochemical Properties. *J. Phys. Chem. C* **2012**, *116*, 16276–16285.
55. Liao, P.; Keith, J. A.; Carter, E. A. Water Oxidation on Pure and Doped Hematite (0001) Surfaces: Prediction of Co and Ni as Effective Dopants for Electrocatalysis. *J. Am. Chem. Soc.* **2012**, *134*, 13296–13309.
56. Ou, J. L.; Chang, C. P.; Sung, Y.; Ou, K. L.; Tseng, C. C.; Ling, H. W.; Ger, M. D. Uniform Polystyrene Microspheres Decorated with Noble Metal Nanoparticles Formed without Using Extra Reducing Agent. *Colloids Surf., A* **2007**, *305*, 36–41.
57. Redel, E.; Mirtchev, P.; Huai, C.; Petrov, S.; Ozin, G. A. Nanoparticle Films and Photonic Crystal Multilayers from Colloidally Stable, Size-Controllable Zinc and Iron Oxide Nanoparticles. *ACS Nano* **2011**, *5*, 2861–2869.